

Measuring topological invariants for higher-order exceptional points in quantum multipartite systems

Pei-Rong Han¹, Wen Ning¹, Xin-Jie Huang¹, Ri-Hua Zheng¹, Shou-Bang Yang¹, Fan Wu¹, Zhen-Biao Yang^{1,2,*}, Qi-Ping Su³, Chui-Ping Yang^{3,†} and Shi-Biao Zheng^{1,2‡}

¹*Department of Physics, Fuzhou University, Fuzhou, Fujian 350108, China*

²*Hefei National Laboratory, Hefei 230088, China*

³*School of Physics, Hangzhou Normal University, Hangzhou 311121, China*

Owing to the presence of exceptional points (EPs), non-Hermitian (NH) systems can display intriguing topological phenomena without Hermitian analogs. However, experimental characterizations of exceptional topological invariants have been restricted to second-order EPs (EP2s) in classical or semiclassical systems. We here propose an NH multi-qubit model with higher-order EPs, each of which is underlain by a multifold-degenerate multipartite entangled eigenstate. We implement the three-qubit model by controllably coupling a superconducting qubit to two microwave resonators, one serving as a Hermitian photonic qubit while the other as an NH qubit. We experimentally quantify the topological invariant for an EP3, by mapping out the complex eigenspectra along a loop surrounding this EP3 in the parameter space. The nonclassicality of the realized topology is manifested by the observed quantum correlations in the corresponding eigenstates. Our results extend research of exceptional topology to fully quantum-mechanical models with multipartite entangled eigenstates. We further demonstrate the non-reciprocal transmission of a single photon, during which the photon is nonlocally shared by three individual elements.

As one of the most well-tested physical theories, quantum mechanics has successfully passed a huge number of experimental tests. In most quantum-mechanical experiments, the system of interest is well isolated from its surrounding environment [1, 2], so that its dynamics is governed by the Schrödinger equation with an energy operator, often called “Hamiltonian”. The Hermiticity of the Hamiltonian ensures that the probability is conserved during the system’s quantum state evolution. However, any real quantum system interacts more or less with the environment [3], which functions by entangling its degrees of freedom with the system’s state [4]. Through this entanglement, the environment continuously monitors the system’s state, which inevitably produces a measurement backaction [5]. Under this disturbance, the system’s dynamics could significantly deviate from the unitary evolution even when it does not exchange any energy with the environment. Mathematically, the state trajectory, associated with this conditional evolution, is also governed by a Schrödinger equation but with a non-Hermitian (NH) Hamiltonian [6].

Due to the non-Hermiticity, two or more eigenvectors of the NH Hamiltonian can coalesce into a single one with the same eigenenergy at exceptional points (EPs) [7, 8]. These singularities can bring about many unique phenomena, exemplified by exotic topological phenomena that are absent in Hermitian systems [8–12]. The past two decades have witnessed a number of experimental explorations on the NH singular features, including spectral parity-time phase transitions [13–21], dynamical chiral behaviors [22–28], exceptional entanglement transitions [29], and NH topology [30–44]. The topology of an NH system can be quantified by some topological invariants, e.g., the winding number [8–12]. So far, such topological invariants have been measured in several experiments, all of which were restricted to second-order EPs (EP2s) realized in classical systems [35–39] or with a classically-driven qubit [40–42]. Compared to EP2s, higher-order EPs can exhibit much richer topological properties [11, 12, 43–45] and the associated spectral topological invariants are defined in a fundamentally different manner [12]. Despite fundamental interest, such invariants have not been unambiguously characterized in experiment.

We here investigate both theoretically and experimentally the quantum-mechanical exceptional topology in an NH composite system consisting of multiple interacting qubits. The topological property associated to each higher-order EP can be quantified by the homotopy invariant, recently proposed by Mandal and Bergholtz [12]. We experimentally engineer the NH three-qubit model in a superconducting circuit, where an Xmon qubit is controllably coupled to two photonic modes stored in two separated microwave resonators. In the single-excitation subspace, each of the two resonators serves as a photonic qubit, and the non-Hermiticity is manifested by the non-negligible photonic dissipation in the lossy resonator. We find that the resulting NH Hamiltonian possesses four EP3s in the real parameter space. We quantify the homotopy invariant associated to the EP3 in the first quadrant of the parameter space, by mapping out the eigenenergies of the NH Hamiltonian along a loop surrounding this EP3. As far as we know, this is the first experimental characterization of the topological invariant associated with a higher-order EP. More importantly, the

observed topology is underlain by quantum-mechanically entangled eigenstates. We further observe a counter-intuitive NH phenomenon, where a photon is unidirectionally localized to the lossless resonator through a nonlocal dynamics.

The system under consideration corresponds to a Heisenberg qubit chain with competing coherent interaction and incoherent dissipation, as shown in Fig. 1a. Under the competition, the system evolution is given by a weighted mixture of infinitely many trajectories, among which of special interest is the one without quantum jump. This trajectory is governed by the following NH Hamiltonian (setting $\hbar = 1$)

$$H = -\frac{1}{2}i \sum_{j=1}^N \kappa_j |1_j\rangle\langle 1_j| + \sum_{j=1}^{N-1} \lambda_j (\sigma_j^+ \sigma_{j+1}^- + H.c.), \quad (1)$$

where $\sigma_j^+ = |1_j\rangle\langle 0_j|$, $\sigma_j^- = |0_j\rangle\langle 1_j|$, $|0_j\rangle$ denotes the ground state of the j th qubit, $|1_j\rangle$ represents its excited state with a decaying rate κ_j , and λ_j denotes the coupling strength between the j th and $(j+1)$ th qubits. The excitation number of the total system is conserved along the no-jump trajectory because the associated excitation-number operator, $N_e = \sum_{j=1}^N |1_j\rangle\langle 1_j|$, commutes with H . Hereafter, we will consider the system behaviors restricted in the single-excitation subspace $\{\sigma_j^+ |0_1 \dots 0_N\rangle\}$ with $j = 1$ to N .

For $\kappa_j = 0$ ($j = 1$ to N), the Hamiltonian of Eq. (1) has N real eigenenergies, which display an N -fold degeneracy for $\lambda_j = 0$. When one or more qubits are subjected to dissipations, the eigenenergies become complex. The resulting spectral structure can display exotic topological features without Hermitian analogues. To clearly illustrate the underlying NH quantum topological physics, we consider a three-qubit system. For simplicity, we assume $\kappa_2 = \kappa_3 = 0$, and drop off the subscript of κ_1 . Fig. 1b (c) shows the maximal real (imaginary) part of the gaps among the three complex eigenenergies versus λ_1 and λ_2 . The results clearly show that the non-Hermiticity splits the real degeneracy into four EP3s at $\{\pm\lambda_1^c, \pm\lambda_2^c\}$ with $\lambda_1^c = \sqrt{2}\kappa/3\sqrt{3}$ and $\lambda_2^c = \kappa/6\sqrt{3}$. At each EP3, the three eigenenergies have a vanishing real part and the same nonzero imaginary part.

The spectrum of the NH Hamiltonian exhibits a rich topological structure, where each of the four EP3s is connected to two curves of EP2s (solid lines in Fig. 1d), at which a pair of eigenstates and eigenenergies coalesce. The details of these eigenenergies are shown in Supplemental Material. Enclosed in the EP2 contour is an isofrequency region, where all the three eigenenergies have the same real part. This is a 2D generalization of the linear-like two-fold degenerate Fermi arc, which connects 2 EP2s existing in a 2D system [30]. In addition to the real Fermi arc, each of the four EP3s emanates an i-Fermi arc (dashed lines in Fig. 1d) [11], along which the imaginary parts are three-fold degenerate. With a global shift of the spectrum by a suitable imaginary value, the four i-Fermi arcs correspond to the regions where the eigenenergies are all real. In view of spectral phase transitions, each of the four EP3s corresponds to a tripoin, where three distinct phases (featuring imaginary, real, and complex energy gaps) meet together.

We perform the experiment using a circuit quantum electrodynamics device with five Xmon qubits, each controllably coupled to the common bus resonator (R_b) of a fixed frequency $\omega_b/2\pi = 5.58$ GHz. The NH quantum multipartite system is realized with one of these qubits (labeled as Q), the bus resonator R_b , and Q 's readout resonator (R_r), which has a frequency $\omega_r/2\pi = 6.66$ GHz. The on-resonance coupling strength between Q and R_b (R_r) is $g_b = 20 \times 2\pi$ MHz ($g_r = 41 \times 2\pi$ MHz). The decaying rate of Q (R_b) is 0.06 MHz (0.08 MHz), which is two orders smaller than that of R_r ($\kappa = 5$ MHz). Thus, the dissipations of Q and R_b are negligible. To realize the NH tripartite Hamiltonian in a controllable manner, two parametric modulations are simultaneously applied to Q to modulate its transition frequency as $\omega_q = \omega_0 + \sum_{j=1,2} \varepsilon_j \cos(\nu_j t)$, where ω_0 is the mean frequency of Q , and ε_j and ν_j respectively denote the

amplitude and frequency of the j th modulation, as depicted in Fig. 2a. Under the condition $\omega_0 + \nu_1 = \omega_r$, the qubit Q interacts with the readout resonator R_r at the first upper sideband for the first modulation, with the strength $\lambda_1 = g_r J_1(\varepsilon_1/\nu_1)$, where $J_1(\mu)$ is the first-order Bessel function of the first kind. The second modulation is used to induce the sideband interaction between Q and R_b , with the effective photonic swapping rate λ_2 controlled by ε_2 . The sideband interactions and the system parameters are detailed in Supplemental Material. In the subspace spanned by the zero- and one-photon states, each of these resonators serves as a photonic qubit, and the R_b - Q - R_r system is equivalent to a three-qubit model. The system dynamics, associated with no-jump trajectory, is described by the NH Hamiltonian (1) with $N = 3$.

The experiment starts with the preparation of an initial single-excitation state, following which the parametric modulations are applied to Q , with the experimental pulse depicted in Fig. 2b. In the experiment, the parametric modulations have tunable frequencies (ν_1, ν_2) and amplitudes ($\varepsilon_1, \varepsilon_2$) for controlling the Q - R_r and Q - R_b couplings. The resulting system dynamics is governed by the NH Hamiltonian of Eq. (1) with $\kappa_2 = \kappa_3 = 0$ and $\kappa_1 = \kappa$. After a preset interaction time t , the parametric modulations are switched off to have Q decoupled from both R_b and R_r .

The system ends in the state

$$|\psi(t)\rangle = c_1(t)|1_b0_q0_r\rangle + c_2(t)|0_b1_q0_r\rangle + c_3(t)|0_b0_q1_r\rangle. \quad (2)$$

Here the subscripts b , q , and r label R_b , Q , and R_r , respectively. The joint tripartite output state is read out with the assistance of two ancilla qubits, denoted as Q_1 and Q_2 . The R_b - Q - R_r output state is mapped to the Q_1 - Q_2 - Q system, which is realized by swapping gates (see Supplemental Material). Bloch vectors of the three qubits along different axes are then measured. By correlating the outcomes of these measurements, the three-qubit density matrix is reconstructed. Removing the ground state element and renormalizing the remaining ones, we obtain the final state of the system evolving under the NH Hamiltonian. With a correction for the infidelity of the state mapping, the resulting Q_1 - Q_2 - Q output state corresponds to the R_b - Q - R_r output state right before the state mapping. Fig. 2c shows the evolutions of the populations $|1_b0_q0_r\rangle$, $|0_b1_q0_r\rangle$, and $|0_b0_q1_r\rangle$ for the initial state $|0_b1_q0_r\rangle$, measured at the point $\lambda_1 = 0.21 \times 2\pi$ MHz and $\lambda_2 = 0.31 \times 2\pi$ MHz. These populations are obtained by discarding the measurement outcome $|0_b0_q0_r\rangle$ and then renormalizing the probabilities for occurrences of the three single-excitation outcomes.

The topological invariant associated with each EP3 can be quantified by the winding number, calculated in terms of the resultant vector \mathcal{R} [12]

$$\mathcal{W} = \sum_{j=1,2} \oint_{C_\lambda} \frac{1}{\|\mathcal{R}\|^2} \left(\mathcal{R}_1 \frac{\partial \mathcal{R}_2}{\partial \lambda_j} - \mathcal{R}_2 \frac{\partial \mathcal{R}_1}{\partial \lambda_j} \right) d\lambda_j, \quad (3)$$

where the integral loop C_λ encloses the EP3 in the 2D parameter space. \mathcal{R}_1 and \mathcal{R}_2 depend upon the eigenenergies (see Supplemental Material for details), which can in principle be extracted from the output states measured for different interaction times. To simplify the measurement, we choose a square-shaped loop on the λ_1 - λ_2 plane. The loop has four vertices $(0, 0)$, $(\lambda_m, 0)$, $(0, \lambda_m)$, and (λ_m, λ_m) , as shown in Fig. 3a. On the edge from $(0, 0)$ to $(\lambda_m, 0)$ and that from $(0, 0)$ to $(0, \lambda_m)$, the system reduces to interacting bipartite models, whose eigenspectrum can be extracted in a relatively easy manner. In our experiment, λ_m is set to be $1 \times 2\pi$ MHz. With this choice, the eigenstates of the NH Hamiltonian on the other two edges are roughly given by those of the Hermitian interaction Hamiltonian, denoted as $|\Phi_j\rangle$ ($j = 1$ to 3). In the basis $\{|\Phi_j\rangle\}$, each off-diagonal elements of the NH term has a magnitude much smaller than the corresponding energy gap, and thus can be treated as a perturbation (see Supplemental Material). As a consequence, one eigenenergy has a zero real part, and the other two have the same imaginary part but opposite real parts. This implies that the number of parameters, which determine the three complex eigenenergies, is reduced by one half. Therefore, the experimental extraction of the eigenenergies is significantly simplified.

The eigenenergies, measured along the four edges of the square-shaped loop, are detailed in Supplemental Material. For different values of λ_1 or λ_2 , \mathcal{R}_1 and \mathcal{R}_2 are calculated from the corresponding measured eigenenergies, as shown in Fig. 3b-e. The dashed lines denote the functions fitted with the measured data. The winding number based on thus-obtained \mathcal{R}_1 and \mathcal{R}_2 is $W = 1$, which confirms that the loop encircles an EP3. In addition to the EP3, the loop surrounds infinitely multiple EP2s, which form two exceptional arcs that cross at the EP3, as illustrated in Fig. 3a. These EP2s have no contribution to the characterized topological invariant, which corresponds to the winding number of the relative angle between \mathcal{R}_1 and \mathcal{R}_2 [12]. This implies that the spectral topological features of higher EPs are fundamentally distinct from those of EP2s. As detailed in Ref. [12], the winding number defined in Eq. (3) is the simplest example of the homotopy invariants, which can quantify topological properties of multifold symmetry-protected EPs but have not been experimentally characterized so far. In a recent acoustic experiment [43], the measured local phase rigidities of the eigenvectors near an EP3 have a critical exponent coinciding with the winding number quantifying the calculated global Berry phase. However, the Berry phase itself, which characterizes the topological charge associated to the eigenvectors, has not been experimentally extracted, neither has the eigenspectral topological invariant. In a recent experiment [49], a third-order exceptional line was observed with a nitrogen-vacancy system, where the NH Hamiltonian for a single electron with three levels was constructed by the dilation method. However, the topological properties of the realized EP3 has not been experimentally characterized.

To reveal the nonclassicality of the eigenstates underlying the eigenspectra, we perform quantum state tomography on the output state of the system. For different values of the control parameters, the evolutions of the measured pairwise concurrences are detailed in Supplemental Material. For the edges $\lambda_1 = 0$ and $\lambda_2 = 0$, the system reduces to a two-qubit model, so that the eigenstates can be extracted from the state evolution in a relatively easy way. At point $(0, \lambda_m)$, the measured concurrences of the two eigenstates ($|\Phi_\pm\rangle$) for the R_b - Q subsystem, which is decoupled from R_r , are 0.997 and 0.997, respectively. At point $(\lambda_m, 0)$, the concurrences for two measured Q - R_r eigenstates ($|\Phi'_\pm\rangle$) are respectively 0.971 and 0.971. When $\lambda_1 \neq 0$ and $\lambda_2 \neq 0$, each of the three eigenenergies is underlain by a tripartite entangled eigenstate, for which each qubit is quantum-mechanically correlated to either of the other two qubits.

Experimental extraction of these eigenstates is a challenging task because each eigenstate involves four parameters to be determined. However, the observation of tripartite entangled states, evolved from the initial product state $|0_b 1_q 0_r\rangle$, indicates that there exists tripartite entanglement in the underlying eigenstates. These observed nonclassical correlations represent another unique feature that fundamentally distinguishes the presently observed topology from those previously demonstrated in classical or semiclassical systems [30–45].

The inherent nonclassical features, together with the NH effects, give rise to a unique single-photon non-reciprocal behavior, which occurs in the regime $\lambda_2 \ll \lambda_1, \kappa$. We first investigate the evolution of the initial product state $|1_b 0_q 0_r\rangle$ with a single photon in R_b , prepared by using an ancilla qubit. After this preparation, the swapping couplings are switched on for a preset time, following which the joint output state is read out. Fig. 4a displays the populations of the states $|1_b 0_q 0_r\rangle$, $|0_b 1_q 0_r\rangle$, and $|0_b 0_q 1_r\rangle$ versus interaction time t . All the results are measured for $\lambda_1 = 1.43 \times 2\pi$ MHz and $\lambda_2 = 0.15 \times 2\pi$ MHz. As expected, the photon almost remains in R_b , indicating that the evolution is frozen. This localization is due to the fact that the Q - R_r coupling produces dressed states with energy shifts much larger than λ_2 . These energy gaps prevent Q from absorbing the photon from R_b .

It should be noted that, even without dissipation, the photon transfer between R_b and Q is also prohibited as long as λ_1 is much larger than λ_2 . To confirm the non-reciprocal nature of the dynamics, we investigate the photon's behavior for the case that the photon is initially stored in R_r . This single-photon state is prepared by performing the transformation $|0_q\rangle \rightarrow |1_q\rangle$ on Q with a π pulse, and then transferring the excitation to R_r through a swapping operation, which is realized with a parametric modulation. Fig. 4b shows the evolutions of the populations of $|1_b 0_q 0_r\rangle$, $|0_b 1_q 0_r\rangle$, and $|0_b 0_q 1_r\rangle$. As expected, these populations behave in a manner fundamentally distinct from those for the initial state $|1_b 0_q 0_r\rangle$, thereby manifesting a unidirectional transmission of the photon from R_r to R_b via the superconducting qubit. This nontrivial behavior originates from the interplay of the R_r 's fast dissipation and the strong Q - R_r coupling. Due to the weak Q - R_b interaction, the photon population is continuously transferred to R_b at a slow rate. Once the photon is re-absorbed by the strongly-coupled Q - R_r subsystem, it quickly leaks into the environment, thus preventing the re-population of the photon in this Q - R_r subsystem. Due to the strong dissipation of $|0_b 0_q 1_r\rangle$, the single-excitation population becomes very small after a long time evolution, so that the oscillation signals are vulnerable to the thermal noises. This vulnerability accounts for the large fluctuations of the data measured after 1 μ s.

To confirm the quantum characteristics of this non-reciprocal behavior, we map out the evolutions of the Q - R_r concurrences, and present the results in Fig. 4c. These results clearly show that the photon is transported through a highly nonclassical process, during which the photon is nonlocally distributed among the three sites. We note that optical non-reciprocity has been realized in semiclassical light-matter systems [46–48], where no quantum entanglement was observed. In distinct contrast, the present unidirectional photonic transmission is a consequence of the NH tripartite entanglement dynamics, during which the photon is simultaneously shared by the two resonators and the Xmon qubit. This nonlocal-dynamics-enabled localization represents an important effect of NH interacting quantum many-body systems, but has not been reported up to today.

In conclusion, we have investigated the exceptional topology in interacting many-body quantum systems, with a competition between coherent couplings and incoherent dissipation. The quantum topology is manifested by the presence of multiple higher-order EPs, each of which carries a quantized topological charge and is associated with a multi-fold degenerate eigenstate displaying highly nonclassical correlations. The NH model is experimentally realized with a superconducting qubit, which is correlated to a lossless bus resonator and a decaying readout resonator by swapping a single photon. The topological charge at each EP3 is quantified by the winding number, extracted from the eigenspectra measured with the assistance of two ancilla qubits. Each of the corresponding eigenstates exhibits quantum entanglement, confirming the nonclassical origin of the topology. We further observe a unique non-reciprocal behavior of the photon, reflected by its unidirectional transmission during the entanglement dynamics.

This work was supported by the National Natural Science Foundation of China (Grant Nos. 12274080, U21A20436) and Innovation Program for Quantum Science and Technology (Grant Nos. 2021ZD0300200, 2021ZD0301705).

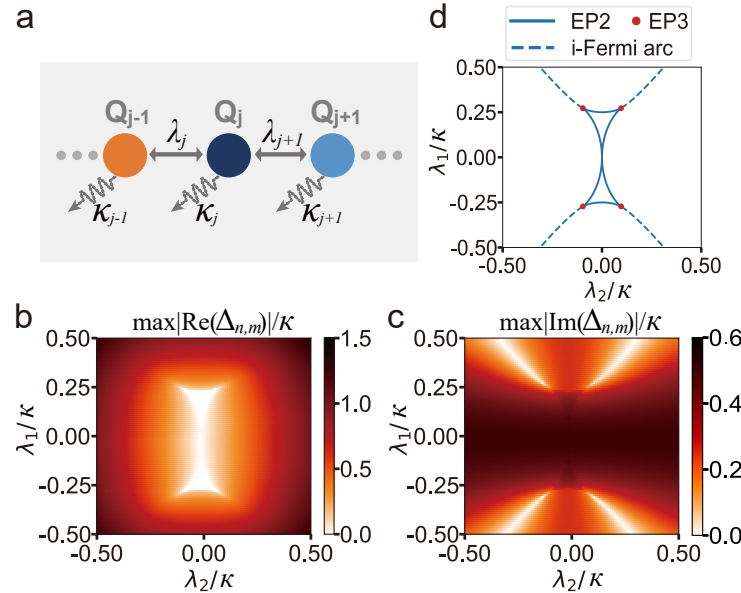


FIG. 1: (color online). Sketch of the NH qubit-spin chain and spectral structure. (a) Theoretical model. The system involves N qubits (Q_j), each serving as a pseudo spin. The NH Hamiltonian dynamics features the competition between the nearest-neighbor swapping couplings (λ_j) and the energy dissipations (κ_j). (b), (c) Maxima for the real (b) and imaginary (c) gaps versus λ_1 and λ_2 in the three-qubit model. For simplicity, we set $\kappa_2 = \kappa_3 = 0$, and assume κ_1 has a fixed nonzero value κ . At the three-fold degeneracy points $\{\pm\lambda_1^c, \pm\lambda_2^c\}$, the maximum gap among the three complex eigenenergies vanishes. Here the parameters λ_1 and λ_2 are scaled in unit of κ . $\Delta_{n,m}$ denotes the difference between two eigenenergies, i.e., $E_n - E_m$ ($n \neq m$, $n, m = 1, 2, 3$). (d) The solid lines denote EP2s where a pair of eigenstates coalesce. Along the dashed lines, all the three eigenenergies have the same imaginary part. Their intersection points (red dots) are EP3s connecting Fermi arcs and i-Fermi arcs.

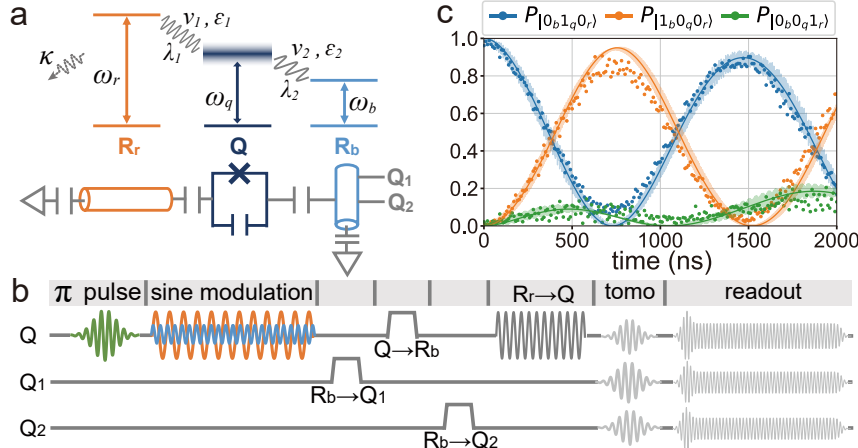


FIG. 2: (color online). Synthesis of the NH three-qubit model. (a) Experimental implementation. The non-Hermitian Hamiltonian is realized in a circuit, where a Josephson-junction-based qubit (Q), together with a bus resonator (R_b) and a readout resonator (R_r), comprises an effective three-qubit model in the single-excitation subspace. The decaying rates of Q and R_b are respectively 0.06 MHz and 0.08 MHz, both of which can be neglected compared to that of R_r , $\kappa = 5$ MHz. Q is coupled to R_r (R_b) at the first upper (lower) sideband with respect to the first (second) parametric modulation. (b) Pulse sequence. The qubit Q is first prepared in the excited state at its idle frequency, followed by the application of two sine modulations. The modulation frequencies (ν_1, ν_2) and amplitudes are tunable for controlling λ_1 and λ_2 . After the modulating pulse, the evolved R_b - Q - R_r output state is mapped to the Q_1 - Q_2 - Q system for readout, where Q_1 and Q_2 are two ancilla qubits, each of which can be controllably coupled to the bus resonator. (c) Observed evolutions of the populations. All data are measured for the initial state $|0_b1_q0_r\rangle$ at the point $\lambda_1 = 0.21 \times 2\pi$ MHz and $\lambda_2 = 0.31 \times 2\pi$ MHz. The results are obtained by discarding the measurement outcome $|0_b0_q0_r\rangle$ and renormalizing the remaining populations of $|1_b0_q0_r\rangle$, $|0_b1_q0_r\rangle$, and $|0_b0_q1_r\rangle$ in the single-excitation subspace. The solid curves are theoretical predictions using the NH Hamiltonian (Eq. 1), while the fast oscillating curves are numerical simulation results using the original Hamiltonian (given in Supplemental material) with frequency modulations included.

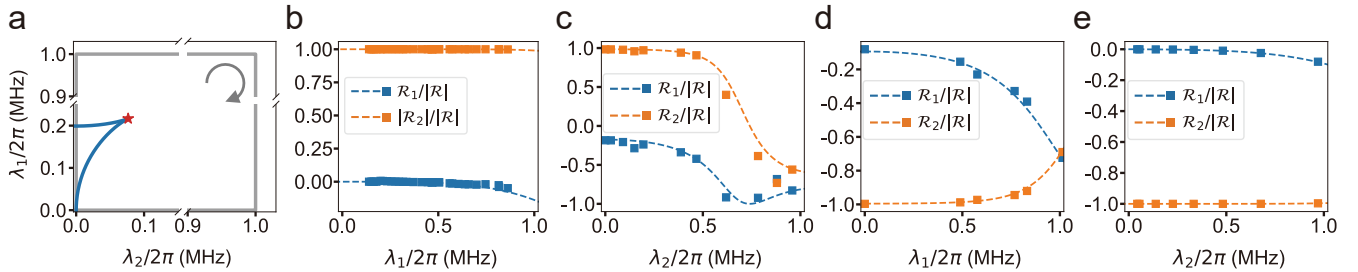


FIG. 3: (color online). Characterization of the NH topology. (a) Loop traversed for extracting the winding number. The loop (gray solid line) is square-shaped with four vertices $(0,0)$, $(\lambda_m,0)$, $(0,\lambda_m)$, and (λ_m,λ_m) , where $\lambda_m = 1 \times 2\pi$ MHz. This loop surrounds an EP3 (red star), which connects two Fermi arcs consisting of EP2s (blue solid line). The arrow denotes the direction of the integral along the loop. (b)-(e) Normalized resultant vectors measured against λ_1 with $\lambda_2 = 0$ (b) and λ_m (d), and against λ_2 with $\lambda_1 = 0$ (c) and λ_m (e). The squares represent the components $\mathcal{R}_1/|\mathcal{R}|$ (blue) and $\mathcal{R}_2/|\mathcal{R}|$ (orange), respectively. The dotted lines denote the fitted $\mathcal{R}_1/|\mathcal{R}|$ and $\mathcal{R}_2/|\mathcal{R}|$ as functions of λ_1 or λ_2 . The winding number, calculated with these fitted functions, is 1.

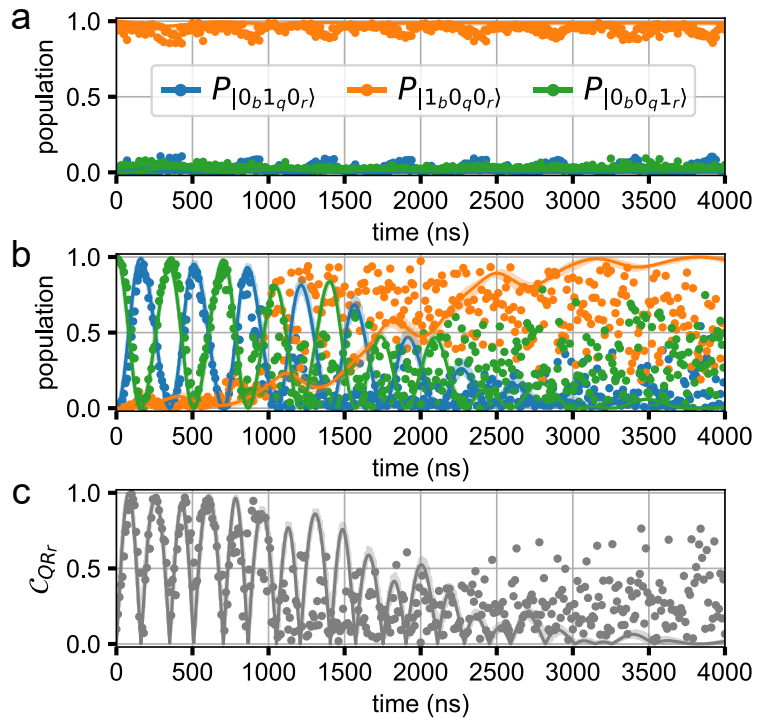


FIG. 4: (color online). Observation of non-reciprocity. (a), (b) Population evolutions for the initial state $|1b0q0r\rangle$ (a) and $|0b0q1r\rangle$ (b). All data are obtained by discarding the null-excitation measurement outcomes and renormalizing the populations in the single-excitation subspace. (c) Evolutions of Q - R_r concurrences for the initial state $|0b0q1r\rangle$. The concurrences are extracted from the reconstructed R_b - Q - R_r output state associated with the no-jump trajectory. All the results are measured for $\lambda_1 = 1.43 \times 2\pi$ MHz and $\lambda_2 = 0.15 \times 2\pi$ MHz. The solid curves are theoretical predictions using the NH Hamiltonian (Eq. 1), while the fast oscillating curves (shadow areas) are numerical simulation results using the original Hamiltonian with frequency modulations included.

* E-mail: zbyangmk@gmail.com

† E-mail: yangcp@hznu.edu.cn

‡ E-mail: fjqiqo@fzu.edu.cn

[1] D. J. Wineland, Nobel Lecture: Superposition, entanglement, and raising Schrödinger's cat, *Rev. Mod. Phys.* **85**, 1103 (2013).

[2] S. Haroche, Nobel Lecture: Controlling photons in a box and exploring the quantum to classical boundary, *Rev. Mod. Phys.* **85**, 1083 (2013).

[3] M. O. Scully and M. S. Zubairy, *Quantum Optics* (Cambridge, 2000).

[4] W. H. Zurek, Decoherence, einselection, and the quantum origins of the classical, *Rev. Mod. Phys.* **75**, 715 (2003).

[5] Y. Ashida, Z. Gong, and M. Ueda, Non-Hermitian physics, *Adv. Phys.* **69**, 249 (2020).

[6] C. M. Bender and S. Boettcher, Real spectra in non-Hermitian Hamiltonians having \mathcal{PT} symmetry, *Phys. Rev. Lett.* **80**, 5243 (1998).

[7] S. K. Özdemir, S. Rotter, F. Nori, and L. Yang, Parity-time symmetry and exceptional points in photonics, *Nat. Mater.* **18**, 783 (2019).

[8] K. Ding, C. Fang, and G. Ma, Non-Hermitian topology and exceptional-point geometries, *Nat. Rev. Phys.* **4**, 745 (2022).

[9] E. J. Bergholtz, J. C. Budich, and F. K. Kunst, Exceptional topology of non-Hermitian systems, *Rev. Mod. Phys.* **93**, 015005 (2021).

[10] Z. Gong, Y. Ashida, K. Kawabata, K. Takasan, S. Higashikawa, and M. Ueda, Topological phases of non-Hermitian systems, *Phys. Rev. X* **8**, 031079 (2018).

[11] I. Mandal and E. J. Bergholtz, Symmetry and higher-order exceptional points, *Phys. Rev. Lett.* **127**, 186601 (2021).

[12] P. Delplace, T. Yoshida, and Y. Hatsugai, Symmetry-protected multifold exceptional points and their topological characterization, *Phys. Rev. Lett.* **127**, 186602 (2021).

[13] Y. Choi, S. Kang, S. Lim, W. Kim, J.-R. Kim, J.-H. Lee, and K. An, Quasieigenstate coalescence in an atom-cavity quantum composite, *Phys. Rev. Lett.* **104**, 153601 (2010).

[14] L. Xiao, K. Wang, X. Zhan, Z. Bian, K. Kawabata, M. Ueda, W. Yi, and P. Xue, Observation of critical phenomena in parity-time-symmetric quantum dynamics, *Phys. Rev. Lett.* **123**, 230401 (2019).

[15] F. E. Öztürk, T. Lappe, G. Hellmann, J. Schmitt, J. Klaers, and F. Vewinger, Observation of a non-Hermitian phase transition in an optical quantum gas, *Science* **372**, 88 (2021).

[16] P. Peng, W. Cao, C. Shen, W. Qu, J. Wen, L. Jiang, and Y. Xiao, Anti-parity-time symmetry with flying atoms, *Nat. Phys.* **12**, 1139 (2016).

[17] J. Li, A. K. Harter, J. Liu, L. d. Melo, Y. N. Joglekar, and L. Luo, Observation of parity-time symmetry breaking transitions in a dissipative Floquet system of ultracold atoms, *Nat. Commun.* **10**, 855 (2019).

[18] Y. Wu, W. Liu, J. Geng, X. Song, X. Ye, C.-K. Duan, X. Rong, and J. Du, Observation of parity-time symmetry breaking in a single-spin system, *Science* **364**, 878 (2019).

[19] M. Naghiloo, M. Abbasi, Y. N. Joglekar, and K. W. Murch, Quantum state tomography across the exceptional point in a single dissipative qubit, *Nat. Phys.* **15**, 1232 (2019).

[20] Z. Wang, Z. Xiang, T. Liu, X. Song, P. Song, X. Guo, L. Su, H. Zhang, Y. Du, and D. Zheng, Observation of the exceptional point in superconducting qubit with dissipation controlled by parametric modulation, *Chin. Phys. B* **30**, 100309 (2021).

[21] T. Gao *et al.*, Observation of non-Hermitian degeneracies in a chaotic exciton-polariton billiard, *Nat. Phys. (London)* **526**, 554 (2015).

[22] X.-L. Zhang, S. Wang, B. Hou, and C. T. Chan, Dynamically encircling exceptional points: In situ control of encircling loops and the role of the starting point, *Phys. Rev. X* **8**, 021066 (2018).

[23] J. Doppler, A. A. Mailybaev, J. Böhm, U. Kuhl, A. Girschik, F. Libisch, T.J. Milburn, P. Rabl, N. Moiseyev, and S. Rotter, Dynamically encircling an exceptional point for asymmetric mode switching, *Nature (London)* **537**, 76 (2016).

[24] H. Xu, D. Mason, L. Jiang, and J. G. E. Harris, Topological energy transfer in an optomechanical system with exceptional points, *Nature (London)* **537**, 80 (2016).

[25] J. W. Yoon *et al.*, Time-asymmetric loop around an exceptional point over the full optical communication band, *Nature (London)* **562**, 86 (2018).

[26] W. Liu, Y. Wu, C.-K. Duan, X. Rong, and J. Du, Dynamically encircling an exceptional point in a real quantum system, *Phys. Rev. Lett.* **126**, 170506 (2021).

[27] W. Gou, T. Chen, D. Xie, T. Xiao, T.-S. Deng, B. Gadway, W. Yi, and B. Yan, Tunable nonreciprocal quantum transport through a dissipative Aharonov-Bohm ring in ultracold atoms, *Phys. Rev. Lett.* **124**, 070402 (2020).

[28] Z. Ren, D. Liu, E. Zhao, C. He, K. K. Pak, J. Li, and G.-B. Jo, Chiral control of quantum states in non-Hermitian spin-orbit-coupled fermions, *Nat. Phys.* **18**, 385 (2022).

[29] P. R. Han, F. Wu, X. J. Huang, H. Z. Wu, C. L. Zou, W. Yi, M. Zhang, H. Li, K. Xu, D. Zheng, H. Fan, J. Wen, Z. B. Yang, and S. B. Zheng, Exceptional entanglement phenomena: Non-Hermiticity meeting non-classicality, *Phys. Rev. Lett.* **131**, 260201 (2023).

[30] C. Dembowski, H.-D. Gräf, H. L. Harney, A. Heine, W. D. Heiss, H. Rehfeld, and A. Richter, Experimental observation of the topological structure of exceptional points, *Phys. Rev. Lett.* **86**, 787 (2001).

[31] H. Zhou, C. Peng, Y. Yoon, C. W. Hsu, K. A. Nelson, L. Fu, J. D. Joannopoulos, M. Soljačić, and B. Zhen, Observation of bulk Fermi arc and polarization half charge from paired exceptional points, *Science* **359**, 1009 (2018).

- [32] A. Cerjan, S. Huang, M. Wang, K. P. Chen, Y. Chong, and M. C. Rechtsman, Experimental realization of a Weyl exceptional ring, *Nat. Photon.* **13**, 623 (2019).
- [33] J. J. Liu, Z. W. Li, Z. G. Chen, W. Tang, A. Chen, B. Liang, G. Ma, and J.-C. Cheng, Experimental realization of Weyl exceptional rings in a synthetic three-dimensional non-Hermitian phononic crystal, *Phys. Rev. Lett.* **129**, 084301 (2022).
- [34] B. Zhen, C. W. Hsu, Y. Igarashi, L. Lu, I. Kaminer, A. Pick, S.-L. Chua, J. D. Joannopoulos, and M. Soljačić, Spawning rings of exceptional points out of Dirac cones, *Nature (London)* **525**, 354 (2015).
- [35] K. Wang, A. Dutt, K. Y. Yang, C. C. Wojcik, J. Vučković and S. Fan, Generating arbitrary topological windings of a non-Hermitian band, *Science* **371**, 1240 (2021).
- [36] K. Wang, A. Dutt, C. C. Wojcik, and S. Fan, Topological complex-energy braiding of non-Hermitian bands, *Nature (London)* **598**, 59 (2021).
- [37] Q. Zhang, Y. Li, H. Sun, X. Liu, L. Zhao, X. Feng, X. Fan, and C. Qiu, Observation of acoustic non-Hermitian Bloch braids and associated topological phase transitions, *Phys. Rev. Lett.* **130**, 017201 (2023).
- [38] W. Tang, K. Ding, and G. Ma, Direct measurement of topological properties of an exceptional parabola, *Phys. Rev. Lett.* **127**, 034301 (2021).
- [39] R. Su, *et al.*, Direct measurement of a non-Hermitian topological invariant in a hybrid light-matter system, *Sci. Adv.* **7**, eabj8905 (2021).
- [40] W. Zhang, X. Ouyang, X. Huang, X. Wang, H. Zhang, Y. Yu, X. Chang, Y. Liu, D.-L. Deng, and L.-M. Duan, Observation of non-Hermitian topology with nonunitary dynamics of solid-state spins, *Phys. Rev. Lett.* **127**, 090501 (2021).
- [41] M.-M. Cao, K. Li, W.-D. Zhao, W.-X. Guo, B.-X. Qi, X.-Y. Chang, Z.-C. Zhou, Y. Xu, and L.-M. Duan, Probing complex-energy topology via non-Hermitian absorption spectroscopy in a trapped ion simulator, *Phys. Rev. Lett.* **130**, 163001 (2023).
- [42] Y. Wu, Y. Wang, X. Ye, W. Liu, C.-K. Duan, Y. Wang, X. Rong, and J. Du, Observation of the knot topology of non-Hermitian systems in a single spin, *Phys. Rev. A* **108**, 052409 (2023).
- [43] W. Tang, X. Jiang, K. Ding, Y.-X. Xiao, Z.-Q. Zhang, C. T. Chan, and G. Ma, Exceptional nexus with a hybrid topological invariant, *Science* **370**, 1077 (2020).
- [44] W. Tang, K. Ding, and G. Ma, Realization and topological properties of third-order exceptional lines embedded in exceptional surfaces, *Nat. Commun.* **14**, 6660 (2023).
- [45] Y. S. S. Patil, J. Höller, P. A. Henry, C. Guria, Y. Zhang, L. Jiang, N. Kralj, N. Read, and J. G. E. Harris, Measuring the knot of non-Hermitian degeneracies and non-commuting braids, *Nature (London)* **607**, 271 (2022).
- [46] S. Zhang, Y. Hu, G. Lin, Y. Niu, K. Xia, J. Gong, and S. Gong, Thermal-motion-induced non-reciprocal quantum optical system, *Nat. Photon.* **12**, 744 (2018).
- [47] X.-X. Hu, Z.-B. Wang, P. Zhang, G.-J. Chen, Y.-L. Zhang, G. Li, X.-B. Zou, T. Zhang, H. X. Tang, C.-H. Dong, G.-C. Guo, and C.-L. Zou, Noiseless photonic non-reciprocity via optically-induced magnetization, *Nat. Commun.* **12**, 2389 (2021).
- [48] Q. Lin, W. Yi, and P. Xue, Manipulating directional flow in a two-dimensional photonic quantum walk under a synthetic magnetic field, *Nat. Commun.* **14**, 6283 (2023).
- [49] Y. Wu, Y. Wang, X. Ye, W. Liu, Z. Niu, C. K. Duan, Y. Wang, X. Rong, and J. Du, Third-order exceptional line in a nitrogen-vacancy spin system, *Nat. Nanotechnol.* (2024).

**Supplementary Materials for
“Measuring topological invariants for higher-order exceptional points in quantum
multipartite systems”**

Pei-Rong Han¹, Wen Ning¹, Xin-Jie Huang¹, Ri-Hua Zheng¹, Shou-Bang Yang¹, Fan Wu¹, Zhen-Biao Yang^{1,2,*}, Qi-Ping Su³, Chui-Ping Yang^{3,†} and Shi-Biao Zheng^{1,2,‡}

¹*Department of Physics, Fuzhou University, Fuzhou, Fujian 350108, China*

²*Hefei National Laboratory, Hefei 230088, China*

³*School of Physics, Hangzhou Normal University, Hangzhou 311121, China*

Contents

S1 . Eigenenergies and eigenstates of the NH three-qubit model	1
S2 . Synthesis of the NH model	3
S3 . State readout	4
S4 . Extraction of eigenenergies	4
S5 . Characterization of the nonclassicality	8
S6 . Derivation of the resultant vector	8
S7 . Extraction of the winding number	9
S8 . Non-reciprocity of the photon transmision	11

S1 . EIGENENERGIES AND EIGENSTATES OF THE NH THREE-QUBIT MODEL

The NH (non-Hermitian) model under consideration involves three qubits with nearest-neighbor couplings. The last qubit has a non-negligible dissipation rate κ , while dissipation rates of the first two qubits are negligible. The system dynamics associated with the no-jump trajectory is governed by the NH Hamiltonian (hereafter setting $\hbar = 1$)

$$H = -\frac{1}{2}i\kappa|1_1\rangle\langle 1_1| + (\lambda_1\sigma_1^+\sigma_2^- + \lambda_2\sigma_2^+\sigma_3^- + \text{H.c.}), \quad (\text{S1})$$

where $\sigma_j^+ = |1_j\rangle\langle 0_j|$ and $\sigma_j^- = |0_j\rangle\langle 1_j|$ ($j = 1$ to 3).

In the single-excitation subspace $\{|1_10_20_3\rangle, |0_11_20_3\rangle, |0_10_21_3\rangle\}$, H has three eigenenergies, given by

$$\begin{aligned} E_1 &= -\frac{i\kappa}{6} - \frac{1}{3}\left(\frac{\xi}{\alpha} + \alpha\right), \\ E_2 &= -\frac{i\kappa}{6} - \frac{1}{3}\left[\left(-\frac{1}{2} + i\frac{\sqrt{3}}{2}\right)\frac{\xi}{\alpha} + \left(-\frac{1}{2} - i\frac{\sqrt{3}}{2}\right)\alpha\right], \end{aligned} \quad (\text{S2})$$

^{*}E-mail: zbyangmk@gmail.com

[†]E-mail: yangcp@hznu.edu.cn

[‡]E-mail: fjqiqo@fzu.edu.cn

and

$$E_3 = -\frac{i\kappa}{6} - \frac{1}{3} \left[\left(-\frac{1}{2} - i\frac{\sqrt{3}}{2} \right) \xi + \left(-\frac{1}{2} + i\frac{\sqrt{3}}{2} \right) \alpha \right], \quad (\text{S3})$$

where

$$\begin{aligned} \xi &= 3\lambda_1^2 + 3\lambda_2^2 - \frac{\kappa^2}{4}, \\ \alpha &= \sqrt[3]{\eta + \sqrt{\eta^2 - \xi^2}}, \end{aligned} \quad (\text{S4})$$

and

$$\eta = -\frac{i\kappa}{4} \left(18\lambda_2^2 - 9\lambda_1^2 + \frac{\kappa^2}{2} \right). \quad (\text{S5})$$

Figure S1(a) illustrates either $\min |\text{Im}(E_n - E_m)|$ or $\min ||E_n| - |E_m||$ versus λ_1 and λ_2 scaled in unit of κ . Outside the colored region, $\min |\text{Im}(E_n - E_m)|$ and $\min ||E_n| - |E_m||$ are both 0. Considering this in conjunction with Fig. 1b of the main text, it can be concluded that there are at least two eigenenergies with equal imaginary parts and opposite real parts. Therefore, outside this colored region, the eigenenergy can be expressed as

$$\begin{aligned} E_1 &= iI_1, \\ E_2 &= R + iI, \\ E_3 &= -R + iI, \end{aligned} \quad (\text{S6})$$

where R , I , and I_1 are real parameters. Figure S1(b) shows the minimum of the scaled gaps $\min |E_n - E_m|/\kappa$ ($n, m = 1$ to 3, $n \neq m$) among three complex eigenenergies versus λ_1 and λ_2 . The curves with $\min |E_n - E_m| = 0$ correspond to lines of EP2s, where two of the three eigenenergies coalesce. The corresponding eigenstates are

$$|\Phi_j\rangle = N_j \{ [E_j(E_j + \frac{i\kappa}{2})] |010_21_3\rangle + \lambda_2(E_j + \frac{i\kappa}{2}) |011_20_3\rangle + \lambda_1\lambda_2 |110_20_3\rangle \} \quad (j = 1, 2, 3), \quad (\text{S7})$$

where N_j is the normalization factor.

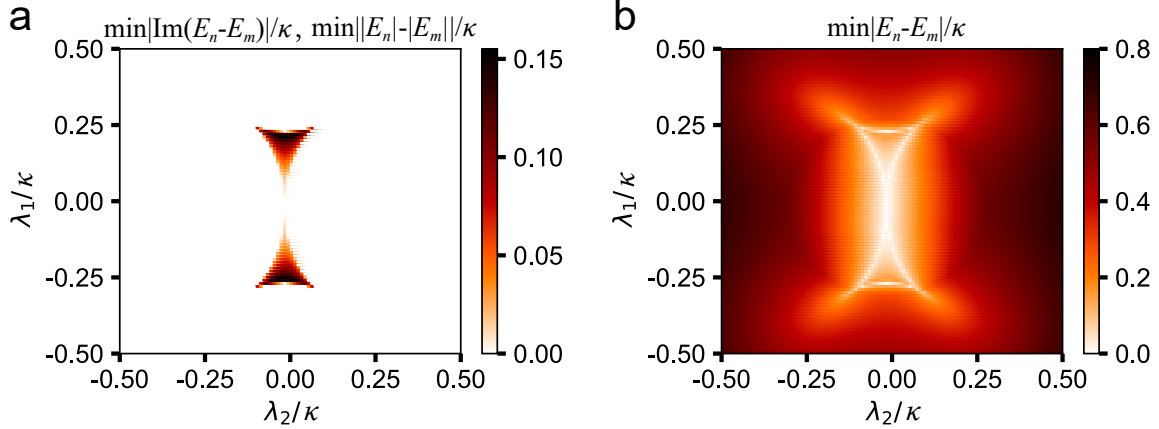


FIG. S1: Characterization of eigenenergies. (a) The colored region is complementary to Fig. 1b in the main text. Outside this region, there is $\min |\text{Im}(E_n - E_m)| = \min ||E_n| - |E_m|| = 0$, indicating that at least two eigenenergies have equal imaginary parts and opposite real parts. (b) The lines of 2EPs are highlighted which corresponds to $\min |E_n - E_m| = 0$.

When $\lambda_1 \neq 0$ and $\lambda_2 \neq 0$, each of these eigenstates is a three-qubit entangled state, for which each qubit is entangled with the other two qubits. The system has four 3EPs at $\{\pm\lambda_1^c, \pm\lambda_2^c\}$ with $\lambda_1^c = \sqrt{2}\kappa/3\sqrt{3}$ and $\lambda_2^c = \kappa/6\sqrt{3}$. For the EP3 in the first quadrant, the three-fold degenerate eigenenergy is

$$E_{\text{EP3}} = -\frac{i\kappa}{6} \quad (\text{S8})$$

with the corresponding eigenstate

$$|\Phi_{EP3}\rangle = -\sqrt{\frac{1}{6}}|0_10_21_3\rangle + i\sqrt{\frac{1}{2}}|0_11_20_3\rangle + \sqrt{\frac{1}{3}}|1_10_20_3\rangle \quad (S9)$$

This three-fold degenerate eigenstate is a genuine tripartite entangled state, manifested by the non-zero pairwise concurrences $\mathcal{C}_{1,2} = \sqrt{\frac{2}{3}}$, $\mathcal{C}_{2,3} = \sqrt{\frac{1}{3}}$, and $\mathcal{C}_{1,3} = \sqrt{\frac{2}{9}}$.

S2 . SYNTHESIS OF THE NH MODEL

The experiment is performed in a circuit quantum electrodynamics architecture involving five frequency-tunable Xmon qubits, each individually coupled to a readout resonator, and all connected to a bus resonator (R_b) with a fixed frequency $\omega_b/2\pi = 5.58$ GHz, as sketched in Fig. S2. The NH three-partite model is synthesized with the bus resonator, one of the Xmon qubits (Q), and its readout resonator (R_r) with a fixed frequency $\omega_r/2\pi = 6.66$ GHz. The R_b - Q and Q - R_r swapping interactions are realized by applying two parametric modulations to Q , making its frequency depend on time as

$$\omega_q = \omega_0 + \varepsilon_1 \cos(\nu_1 t) + \varepsilon_2 \cos(\nu_2 t), \quad (S10)$$

where ω_0 is the mean frequency, and ε_j and ν_j ($j = 1, 2$) are the corresponding modulation amplitude and angular frequency of the j th modulation, respectively. The coherent Hamiltonian of the total system is given by

$$H = H_0 + H_I, \quad (S11)$$

where

$$H_0 = \omega_b a_b^\dagger a_b + \omega_r a_r^\dagger a_r + \omega_q |e\rangle \langle e|, \quad (S12)$$

and

$$H_I = |0_q\rangle \langle 1_q| (g_b a_b^\dagger + g_r a_r^\dagger) + \text{H.c.}, \quad (S13)$$

where a_r^\dagger (a_b^\dagger) and a_r (a_b) denote the creation and annihilation operators for the photonic field stored in R_r (R_b), $|0_q\rangle$ and $|1_q\rangle$ denote the ground and first excited states of Q , and g_b (g_r) is the on-resonance R_b - Q (Q - R_r) coupling strength.

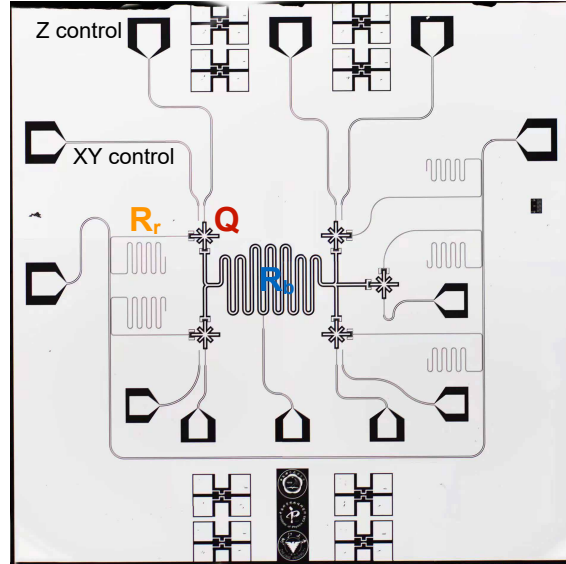


FIG. S2: Circuit diagram.

Performing the transformation $e^{i \int_0^t H_0 dt}$, we obtain the system Hamiltonian in the interaction picture,

$$H'_I = e^{-i\mu_1 \sin(\nu_1 t)} e^{-i\mu_2 \sin(\nu_2 t)} |0_q\rangle \langle 1_q| (e^{i\delta_b t} g_b a_b^\dagger + e^{i\delta_r t} g_r a_r^\dagger) + \text{H.c.}, \quad (\text{S14})$$

where $\mu_j = \varepsilon_j / \nu_j$ ($j = 1, 2$), $\delta_b = \omega_b - \omega_0$, and $\delta_r = \omega_r - \omega_0$. Using the Jacobi-Anger expansion

$$e^{-i\mu_j \sin(\nu_j t)} = \sum_{n=-\infty}^{\infty} J_n(\mu_j) e^{-in\nu_j t}, \quad (\text{S15})$$

with $J_n(\mu_j)$ being the n th Bessel function of the first kind, H'_I can be rewritten as

$$H'_I = \sum_{m,n=-\infty}^{\infty} J_m(\mu_1) J_n(\mu_2) e^{-im\nu_1 t} e^{-in\nu_2 t} |0_q\rangle \langle 1_q| (e^{i\delta_b t} g_b a_b^\dagger + e^{i\delta_r t} g_r a_r^\dagger) + \text{H.c.} \quad (\text{S16})$$

Under the conditions $\nu_1 = \delta_r$ and $\nu_2 = -\delta_b$, Q is resonantly coupled to R_r (R_b) at the first upper (lower) sideband with respect to the first (second) modulation. When $g_b, g_r \ll \nu_1, \nu_2$, the fast-oscillating terms can be discarded, so that H'_I reduces to

$$H'_I = |0_q\rangle \langle 1_q| (\lambda_1 a_b^\dagger + \lambda_2 a_r^\dagger) + \text{H.c.}, \quad (\text{S17})$$

where $\lambda_1 = g_r J_1(\mu_1) J_0(\mu_2)$ and $\lambda_2 = g_b J_0(\mu_1) J_1(\mu_2)$. In the single-excitation subspace, a_b^\dagger and a_r^\dagger can be replaced by $|1_b\rangle \langle 0_b|$ and $|1_r\rangle \langle 0_r|$, respectively. Then H'_I is equivalent to the Hermitian part of the Hamiltonian (1) of the main text with $N = 3$. In our system, the dissipation rates of R_b and Q are respectively 0.08 MHz and 0.06 MHz, which are negligible compared with that of R_r . With the dissipation being included, the NH Hamiltonian is given by Eq. (S1), with R_r , Q , and R_b corresponding to the first, second, and last qubits, respectively.

S3 . STATE READOUT

The readout of the output R_b - Q - R_r state is enabled with two ancilla qubits, denoted as Q_1 and Q_2 . After the NH Hamiltonian dynamics, the state of R_b is mapped to Q_1 through a swapping gate, which is realized by tuning the transition frequency of Q_1 to ω_b for a duration $t_{sw} = \pi/(2g_1) \simeq 12.3$ ns, with $g_1 = 20.3 \times 2\pi$ MHz being the R_b - Q photonic swapping rate. Then, the state of Q is transferred to Q_2 by subsequently performing the Q - R_b and R_b - Q_2 swapping gates. Finally, R_r 's state is transferred to Q . As the maximum frequency of Q ($6.01 \times 2\pi$ GHz) is smaller than ω_r by an amount much larger than g_r , it is necessary to use the parametric modulation to realize the R_r - Q mapping. The corresponding gate duration is 150 ns. With a correction for the state distortion during the state mapping, the resulting Q_1 - Q_2 - Q output state corresponds to the R_b - Q - R_r output state right before the state mapping.

S4 . EXTRACTION OF EIGENENERGIES

In our experiment, we choose a square-shaped loop on the λ_1 - λ_2 plane to extract the winding number. The four vertices of the rectangle are $(0, 0)$, $(\lambda_m, 0)$, $(0, \lambda_m)$, and (λ_m, λ_m) with $\lambda_m \simeq 1 \times 2\pi$ MHz. Along the edge with $\lambda_1 = 0$, R_r is decoupled from the Q - R_b subsystem. In the interaction picture, the Q - R_b swapping coupling is described by the Hamiltonian

$$\mathcal{H} = \lambda_2 (a_b^\dagger |0_q\rangle \langle 1_q| + a_b |1_q\rangle \langle 0_q|), \quad (\text{S18})$$

where a_b^\dagger and a_b denote the creation and annihilation operators for the photonic mode stored in R_b , and $|0_q\rangle$ and $|1_q\rangle$ represent Q 's ground and excited states. In the single-excitation subspace, this Hamiltonian has two eigenenergies $E_{\pm} = \pm\lambda_2$. The corresponding eigenstates are

$$|\Phi_{\pm}\rangle = \frac{1}{\sqrt{2}} (|0_b 1_q\rangle \pm |1_b 0_q\rangle). \quad (\text{S19})$$

The subsystem, starting from the initial state $|0_b 1_q\rangle$, evolves as

$$\cos(\lambda_2 t) |0_b 1_q\rangle - i \sin(\lambda_2 t) |1_b 0_q\rangle. \quad (\text{S20})$$

The value of λ_2 , which depends on the amplitude and frequency of the parametric modulation used to mediate the sideband interaction, is inferred from the observed Rabi oscillation. The population evolutions for the state $|0_b 1_q\rangle$, observed for different values of λ_2 , are presented in Fig. S3(a). The $Q\text{-}R_b$ concurrences associated with the two eigenstates $|\Phi_{\pm}\rangle$, extracted at $\lambda_2 = \lambda_m$, are 0.997 and 0.997, respectively.

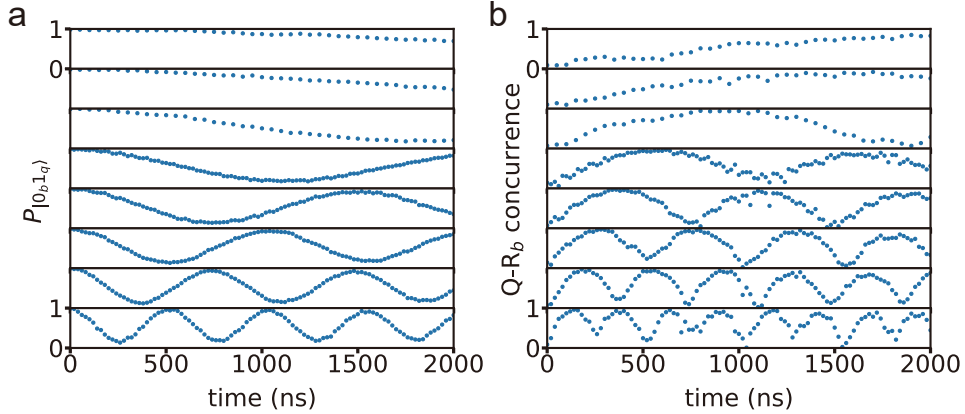


FIG. S3: The population (a) and concurrence (b) evolutions for different values of λ_2 when $\lambda_1 = 0$, i.e. the edge from $(0, 0)$ to $(0, \lambda_m)$.

For $\lambda_2 = 0$, R_b is decoupled from the $Q\text{-}R_r$ subsystem. In this case, the evolution of the $Q\text{-}R_r$ subsystem associated with the no-jump trajectory is described by the NH Hamiltonian

$$\mathcal{H}' = \lambda_1 (a_r^\dagger |0_q\rangle \langle 1_q| + a_r |1_q\rangle \langle 0_q|) - \frac{i}{2} \kappa a_r^\dagger a_r, \quad (\text{S21})$$

where a_r^\dagger (a_r) is the photonic creation (annihilation) operator for R_r . In the single-excitation subspace, the \mathcal{H}' has two eigenenergies

$$E'_\pm = -i\kappa/4 \pm \sqrt{\lambda_1^2 - \kappa^2/16}. \quad (\text{S22})$$

The corresponding eigenstates are

$$|\Phi'_\pm\rangle = \mathcal{N}_\pm \left(|1_q 0_r\rangle + \frac{E'_\pm}{\lambda_1} |0_q 1_r\rangle \right), \quad (\text{S23})$$

where $\mathcal{N}_\pm = \left(1 + |E'_\pm/\lambda_1|^2 \right)^{-1/2}$. Fig. S4(a) shows the measured population of the state $|1_q 0_r\rangle$ versus λ_1 and t . This population is obtained by discarding the outcome $|0_q 0_r\rangle$, and then renormalizing the probabilities for the outcomes of $|1_q 0_r\rangle$ and $|0_q 1_r\rangle$. The gap of the two eigenenergies versus λ_1 , extracted from the population evolution, are shown in Fig. S4(c).

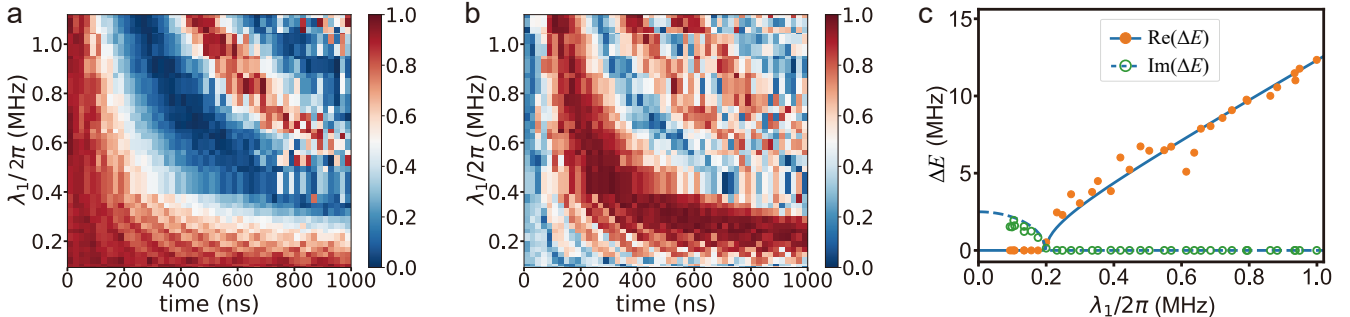


FIG. S4: The population (a) and concurrence (b) evolutions for different values of λ_1 when $\lambda_2 = 0$, i.e. the edge from $(0, 0)$ to $(\lambda_m, 0)$. (c) Spectral gap ΔE . The solid and dashed lines denote the real and imaginary parts, respectively.

When $\lambda_1 \neq 0$ and $\lambda_2 \neq 0$, the evolution of the R_b - Q - R_r system associated with the no-jump trajectory is governed by the Hamiltonian

$$\mathcal{H} = \mathcal{H}^H + \mathcal{H}^{NH}, \quad (\text{S24})$$

where

$$\begin{aligned} \mathcal{H}^H &= |1_q\rangle\langle 0_q| (\lambda_1 a_r + \lambda_2 a_b) + \text{H.c.}, \\ \mathcal{H}^{NH} &= -\frac{1}{2}i\kappa a_r^\dagger a_r. \end{aligned} \quad (\text{S25})$$

Suppose that the loop on the $\lambda_1 - \lambda_2$ plane is a rectangle with four vertices $(0, 0)$, $(\lambda_m, 0)$, $(0, \lambda_m)$, and (λ_m, λ_m) . On the edges from $(0, 0)$ to $(\lambda_m, 0)$ and to $(0, \lambda_m)$, the system reduces to a two-partite model, so that the eigenspectra can be extracted relatively easily. Without dissipation, the three eigenstates of \mathcal{H}^H on the other two edges are given by

$$\begin{aligned} |\Phi_1\rangle &= \sin \theta |1_b 0_q 0_r\rangle - \cos \theta |0_b 0_q 1_r\rangle, \\ |\Phi_2\rangle &= \frac{1}{\sqrt{2}}(\cos \theta |1_b 0_q 0_r\rangle + \sin \theta |0_b 0_q 1_r\rangle + |0_b 1_q 0_r\rangle), \\ |\Phi_3\rangle &= \frac{1}{\sqrt{2}}(\cos \theta |1_b 0_q 0_r\rangle + \sin \theta |0_b 0_q 1_r\rangle - |0_b 1_q 0_r\rangle), \end{aligned} \quad (\text{S26})$$

where $\tan \theta = \lambda_1 / \lambda_2$. The corresponding eigenenergies are $E_1^H = 0$ and $E_2^H = -E_3^H = \lambda$, with $\lambda = \sqrt{\lambda_1^2 + \lambda_2^2}$.

In the basis $\{|\Phi_j\rangle\}$ ($j = 1, 2, 3$), \mathcal{H}^{NH} can be expressed as

$$\mathcal{H}^{NH} = \mathcal{H}^{dg} + \mathcal{H}^{ndg}, \quad (\text{S27})$$

where \mathcal{H}^{dg} and \mathcal{H}^{ndg} represent the diagonal and off-diagonal parts respectively, given by

$$\mathcal{H}^{dg} = \begin{pmatrix} -i\frac{\kappa}{2} \cos^2 \theta & 0 & 0 \\ 0 & -i\frac{\kappa}{4} \sin^2 \theta & 0 \\ 0 & 0 & -i\frac{\kappa}{4} \sin^2 \theta \end{pmatrix}, \quad (\text{S28})$$

and

$$\mathcal{H}^{ndg} = \begin{pmatrix} 0 & i\frac{\kappa}{4\sqrt{2}} \sin(2\theta) & i\frac{\kappa}{4\sqrt{2}} \sin(2\theta) \\ i\frac{\kappa}{4\sqrt{2}} \sin(2\theta) & 0 & i\frac{\kappa}{4} \sin^2 \theta \\ i\frac{\kappa}{4\sqrt{2}} \sin(2\theta) & i\frac{\kappa}{4} \sin^2 \theta & 0 \end{pmatrix}. \quad (\text{S29})$$

In the basis $\{|\Phi_j\rangle\}$, we can rewrite the total Hamiltonian as

$$\mathcal{H} = \mathcal{H}^0 + \mathcal{H}^{ndg}, \quad (\text{S30})$$

where

$$\begin{aligned} \mathcal{H}^0 &= \mathcal{H}^H + \mathcal{H}^{dg} \\ &= \begin{pmatrix} -i\frac{\kappa}{2} \cos^2 \theta & 0 & 0 \\ 0 & \lambda - i\frac{\kappa}{4} \sin^2 \theta & 0 \\ 0 & 0 & -\lambda - i\frac{\kappa}{4} \sin^2 \theta \end{pmatrix}. \end{aligned} \quad (\text{S31})$$

We note \mathcal{H}^{ndg} can be treated as a perturbation, which is explained as follow. On the edge with $\lambda_1 = \lambda_m$, θ changes from $\pi/2$ to $\pi/4$. For $\theta = \pi/2$, the non-zero off-diagonal elements are $\mathcal{H}_{2,3}^{ndg}$ and $\mathcal{H}_{3,2}^{ndg}$, which have a magnitude of $|\mathcal{H}_{2,3}^{ndg}| = \kappa/4$. The ratio of this magnitude to the gap between the last two eigenvalues of \mathcal{H}^0 is $|\mathcal{H}_{2,3}^{ndg}| / |\mathcal{H}_{2,2}^0 - \mathcal{H}_{3,3}^0| = \kappa/8\lambda \simeq 0.099$. When θ changes to $\pi/4$, $|\mathcal{H}_{2,3}^{ndg}| / |\mathcal{H}_{2,2}^0 - \mathcal{H}_{3,3}^0|$ monotonously decreases to 0.070, while $|\mathcal{H}_{1,2}^{ndg}| / |\mathcal{H}_{1,1}^0 - \mathcal{H}_{2,2}^0|$ approximately increases to $\kappa/(4\sqrt{2}\lambda) \simeq 0.099$. On the edge with $\lambda_2 = \lambda_m$, θ

changes from 0 to $\pi/4$. For $\theta = 0$, all the off-diagonal elements are 0. When θ increases to $\pi/4$, $|\mathcal{H}_{1,2}^{ndg}| / |\mathcal{H}_{1,1}^0 - \mathcal{H}_{2,2}^0|$ and $|\mathcal{H}_{2,3}^{ndg}| / |\mathcal{H}_{2,2}^0 - \mathcal{H}_{3,3}^0|$ approximately increase to 0.098 and 0.099, respectively. These results imply that the magnitude of each off-diagonal element is much smaller than the corresponding energy gap, which ensures the perturbation condition. To the first order correction, the three eigenenergies correspond to the diagonal elements of \mathcal{H}^0 . This indicates that the real part of the first eigenenergy E_1 is approximately zero, and the other two eigenenergies E_2 and E_3 have the same imaginary part but opposite real parts. Therefore, the three eigenenergies can be approximately expressed as

$$\begin{aligned} E_1 &\simeq -iI_1, \\ E_2 &\simeq R - iI_2, \\ E_3 &\simeq -R - iI_2, \end{aligned} \quad (\text{S32})$$

where R , I_1 , and I_2 are real parameters, with $I_1 = \frac{\kappa}{2} \cos^2 \theta$ and $I_2 = \frac{\kappa}{4} \sin^2 \theta$. Consequently, the eigenenergies are determined by these three parameters $\{R, I_1, I_2\}$, which can be extracted through observation of the population evolutions.

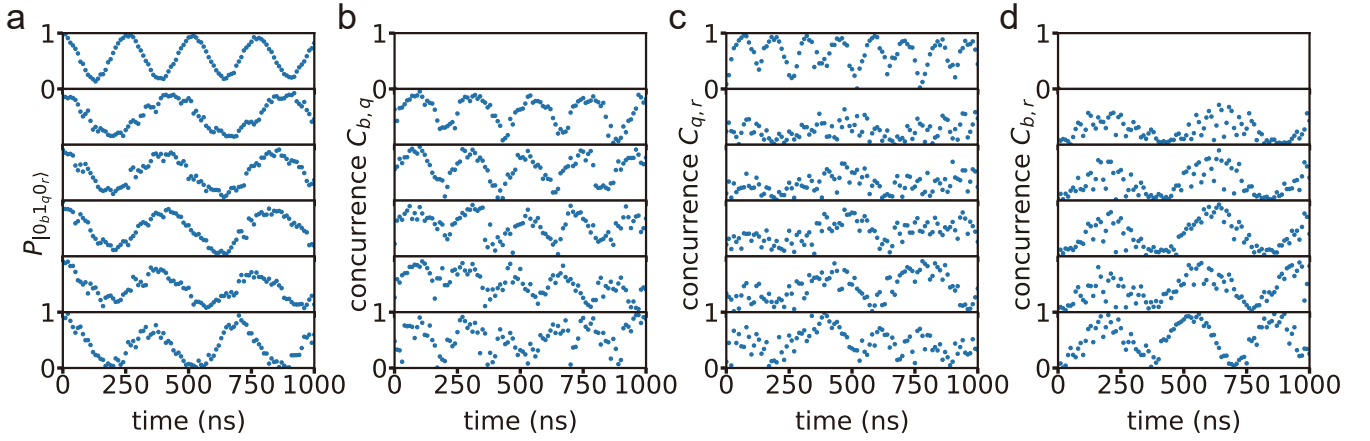


FIG. S5: The population (a) and concurrence (b),(c),(d) evolutions for different values of λ_1 when $\lambda_2 = \lambda_m$, i.e. the edge from $(0, \lambda_m)$ to (λ_m, λ_m) .

Figure S5(a) displays the measured population of the state $|0_b1_q0_r\rangle$ versus λ_1 and t for the edge with $\lambda_2 = \lambda_m$. This population is obtained by discarding the outcome $|0_b0_q0_r\rangle$, and then renormalizing the probabilities of the three single-excitation outcomes. The eigenenergies in terms of R and ΔI ($= |I_1 - I_2|$) versus λ_1 , extracted from this population evolution, are displayed in Fig. S6(a). Figure S9(a) shows the measured $|0_b1_q0_r\rangle$ -state population versus λ_2 and t for the edge with $\lambda_1 = \lambda_m$. The extracted eigenenergies in terms of R and ΔI versus λ_2 are displayed in Fig. S6(b).

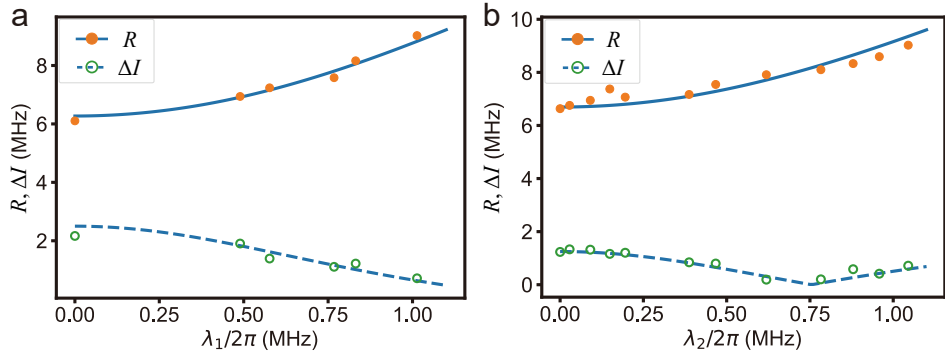


FIG. S6: The extracted eigenenergies in terms of R and ΔI versus (a) λ_1 and (b) λ_2 .

S5 . CHARACTERIZATION OF THE NONCLASSICALITY

Along the edge with $\lambda_1 = 0$, R_r remains in the ground state $|0_r\rangle$. The measured Q - R_b concurrence, versus λ_2 and t , is displayed in Fig. S3(b). The density matrices for the two eigenstates $|\Phi_{\pm}\rangle$, extracted from the data measured at $\lambda_2 = \lambda_m$, are presented in Fig. S7. The concurrences corresponding to these two eigenstates are 0.997 and 0.997, respectively. Fig. S4(b) shows the Q - R_r concurrence versus λ_1 and t , measured for the edge $\lambda_2 = 0$. The measured density matrices, associated with the two eigenstates $|\Phi'_{\pm}\rangle$ for $\lambda_1 = \lambda_m$, are presented in Fig. S8, with the concurrences 0.971 and 0.971.

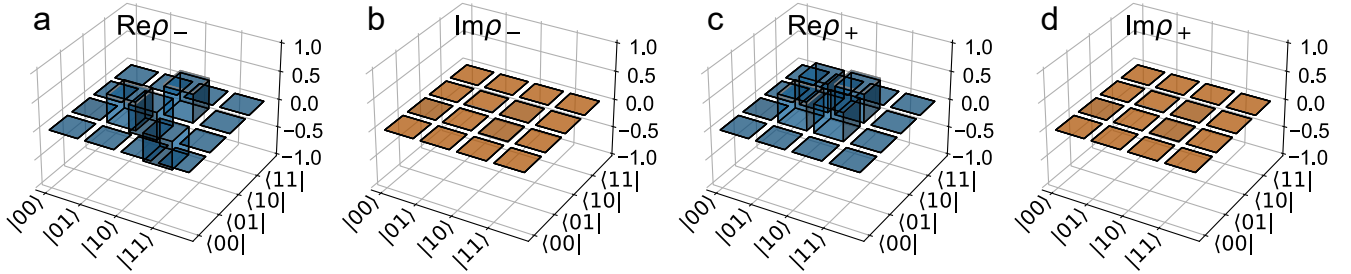


FIG. S7: The density matrices ρ_{\pm} for the two eigenstates $|\Phi_{\pm}\rangle$. (a) The real parts of ρ_- . (b) The imaginary parts of ρ_- . (c) The real parts of ρ_+ . (d) The imaginary parts of ρ_+ . The two numbers in each ket denote the excitation numbers of the qubit and the bus resonator, respectively. The black frames denote the matrix elements of the ideal eigenstates.

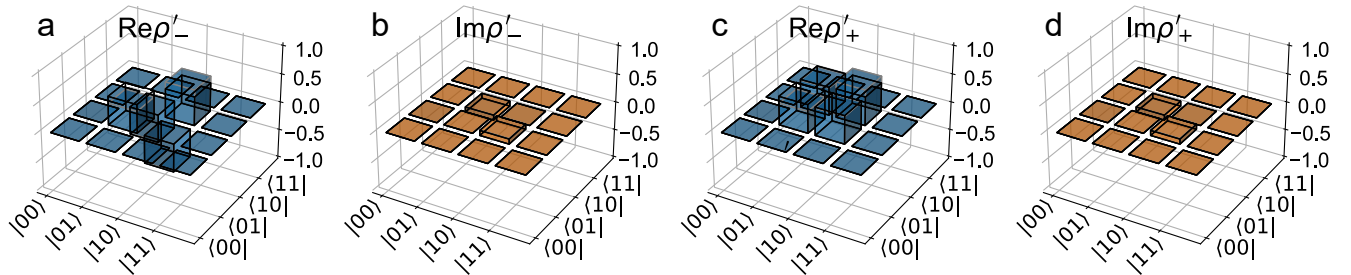


FIG. S8: The density matrices ρ'_{\pm} for the two eigenstates $|\Phi'_{\pm}\rangle$. (a) The real parts of ρ'_- . (b) The imaginary parts of ρ'_- . (c) The real parts of ρ'_+ . (d) The imaginary parts of ρ'_+ . The two numbers in each ket denote the excitation numbers of the qubit and the readout resonator, respectively. The black frames denote the matrix elements of the ideal eigenstates.

Figures S5(b), (c), and (d) present the measured three pairwise concurrences $C_{b,q}$, $C_{q,r}$, and $C_{b,r}$ versus λ_1 and t for the edge with $\lambda_2 = \lambda_m$, where the subscript “ b ”, “ q ”, and “ r ” denote the bus resonator, Xmon qubit, and readout resonator, respectively. Figure S9(b), (c), and (d) showcase the three pairwise concurrences versus λ_2 and t for the edge with $\lambda_1 = \lambda_m$. These results show that the tripartite system evolves from the initial product state $|0_b1_q0_r\rangle$ to a tripartite entangled state under the NH Hamiltonian when $\lambda_1 \neq 0$ and $\lambda_2 \neq 0$. For example, the three concurrences, measured at the point with $\lambda_1 = \lambda_2 = \lambda_m$ for the time 600 ns, are $C_{b,q} = 0.50$, $C_{q,r} = 0.64$, and $C_{b,r} = 0.74$, respectively. These results imply that the corresponding eigenstates are highly-nonclassical states, featuring tripartite quantum entanglement.

S6 . DERIVATION OF THE RESULTANT VECTOR

The resultant is a basic concept in algebra. It can be used to determine whether two polynomials have common roots, defined as

$$R_{P_1, P_2} \equiv \det S_{P_1, P_2}, \quad (\text{S33})$$

where P_1 , P_2 are two polynomials and S_{P_1, P_2} is their Sylvester matrix. Suppose

$$\begin{aligned} P_1 &= a_0 x^n + a_1 x^{n-1} + \dots + a_n, \\ P_2 &= b_0 x^m + b_1 x^{m-1} + \dots + b_m, \end{aligned} \quad (\text{S34})$$

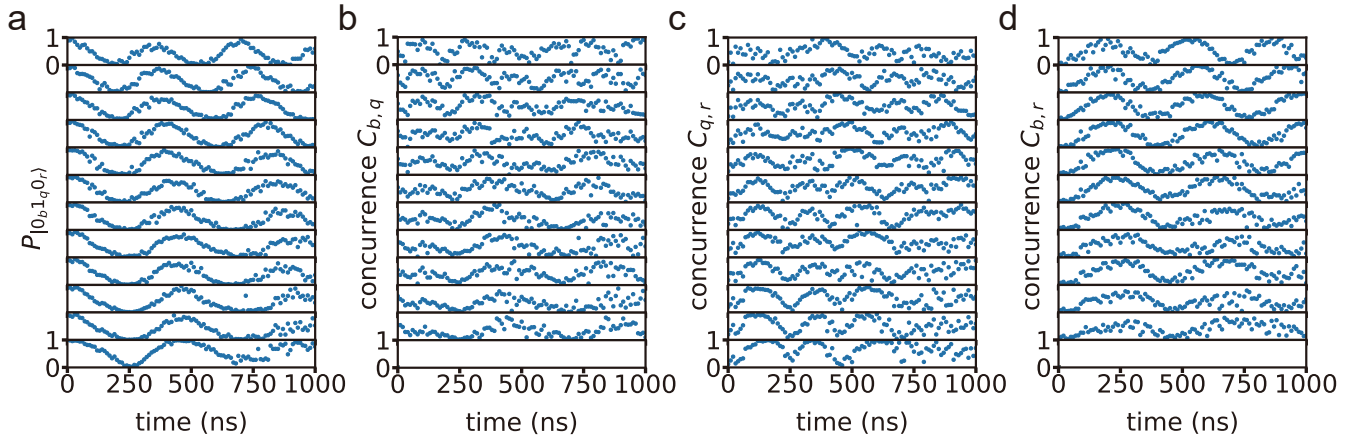


FIG. S9: The population (a) and concurrence (b),(c),(d) evolutions for different values of λ_2 when $\lambda_1 = \lambda_m$, i.e. the edge from $(\lambda_m, 0)$ to (λ_m, λ_m) .

the corresponding resultant is a determinant of order $m + n$,

$$R_{P_1, P_2} = \begin{vmatrix} a_0 & a_1 & a_2 & \dots & \dots & a_n & 0 & \dots & 0 \\ 0 & a_0 & a_1 & \dots & \dots & a_{n-1} & a_n & \dots & 0 \\ \vdots & \vdots \\ 0 & 0 & \dots & 0 & a_0 & \dots & \dots & \dots & a_n \\ b_0 & b_1 & b_2 & \dots & \dots & \dots & b_m & \dots & 0 \\ 0 & b_0 & b_1 & \dots & \dots & \dots & b_{m-1} & b_m & \dots \\ \vdots & \vdots \\ 0 & \dots & 0 & b_0 & b_1 & \dots & \dots & \dots & b_m \end{vmatrix}. \quad (\text{S35})$$

If $R_{P_1, P_2} = 0$, the polynomials P_1 and P_2 have common roots.

For a three-dimensional system governed by the Hamiltonian H , the characteristic polynomial P is given by

$$P = -(E - E_1)(E - E_2)(E - E_3), \quad (\text{S36})$$

where E_1 , E_2 and E_3 are the three eigenvalues of H . The first- and second-order derivatives of $P(E)$ are

$$P' = -[(E - E_1)(E - E_2) + (E - E_2)(E - E_3) + (E - E_3)(E - E_1)], \quad (\text{S37})$$

and

$$P'' = -2[(E - E_1) + (E - E_2) + (E - E_3)]. \quad (\text{S38})$$

The two components of the resultant vector are given by

$$\mathcal{R}_1 = R_{P, P'} = -(E_1 - E_2)^2(E_1 - E_3)^2(E_2 - E_3)^2 \quad (\text{S39})$$

and

$$\mathcal{R}_2 = R_{P, P''} = -8i(E_1 + E_3 - 2E_2)(E_1 + E_3 - 2E_3)(E_2 + E_3 - 2E_1). \quad (\text{S40})$$

Therefore, we can calculate \mathcal{R}_1 and \mathcal{R}_2 at each point (λ_1, λ_2) of the parameter space with the measured eigenenergies. The results are presented in Fig. 3 of the main text.

S7 . EXTRACTION OF THE WINDING NUMBER

The winding number, associated with each EP3, is calculated along a loop enclosing the EP3,

$$\mathcal{W} = \sum_{j=1,2} \oint_{C_\lambda} F(\mathcal{R}_1, \mathcal{R}_2) d\lambda_j, \quad (\text{S41})$$

where the integrand is given by

$$F(\mathcal{R}_1, \mathcal{R}_2) = \frac{1}{\|\mathcal{R}\|^2} \left(\mathcal{R}_1 \frac{\partial \mathcal{R}_2}{\partial \lambda_j} - \mathcal{R}_2 \frac{\partial \mathcal{R}_1}{\partial \lambda_j} \right). \quad (\text{S42})$$

The square-shaped loop chosen in our experiment encloses the EP3 in the first quadrant. Only one control parameter changes along each edge of the loop. Thus the integral can be rewritten as

$$\begin{aligned} \mathcal{W} = & \int_0^{\lambda_m} F(\mathcal{R}_1, \mathcal{R}_2) d\lambda_1 |_{\lambda_2=0} \\ & + \int_0^{\lambda_m} F(\mathcal{R}_1, \mathcal{R}_2) d\lambda_2 |_{\lambda_1=\lambda_m} \\ & + \int_{\lambda_m}^0 F(\mathcal{R}_1, \mathcal{R}_2) d\lambda_1 |_{\lambda_2=\lambda_m} \\ & + \int_{\lambda_m}^0 F(\mathcal{R}_1, \mathcal{R}_2) d\lambda_2 |_{\lambda_1=0}, \end{aligned} \quad (\text{S43})$$

where $F(\mathcal{R}_1, \mathcal{R}_2)$ along the four edges are displayed in Fig. S10.

For simplicity, the square-shaped trajectory can be represented by the parametric equation

$$\begin{aligned} \lambda_1 &= \frac{1}{2}(1 - \cos \theta |\cos \theta| + \sin \theta |\sin \theta|), \\ \lambda_2 &= \frac{1}{2}(1 - \cos \theta |\cos \theta| - \sin \theta |\sin \theta|), \end{aligned} \quad (\text{S44})$$

where θ ranges from 0 to 2π . In this case, the winding number in terms of θ is given by

$$\mathcal{W} = \int_0^{2\pi} \frac{1}{\|\mathcal{R}\|^2} \left(\mathcal{R}_1 \frac{\partial \mathcal{R}_2}{\partial \theta} - \mathcal{R}_2 \frac{\partial \mathcal{R}_1}{\partial \theta} \right) d\theta. \quad (\text{S45})$$

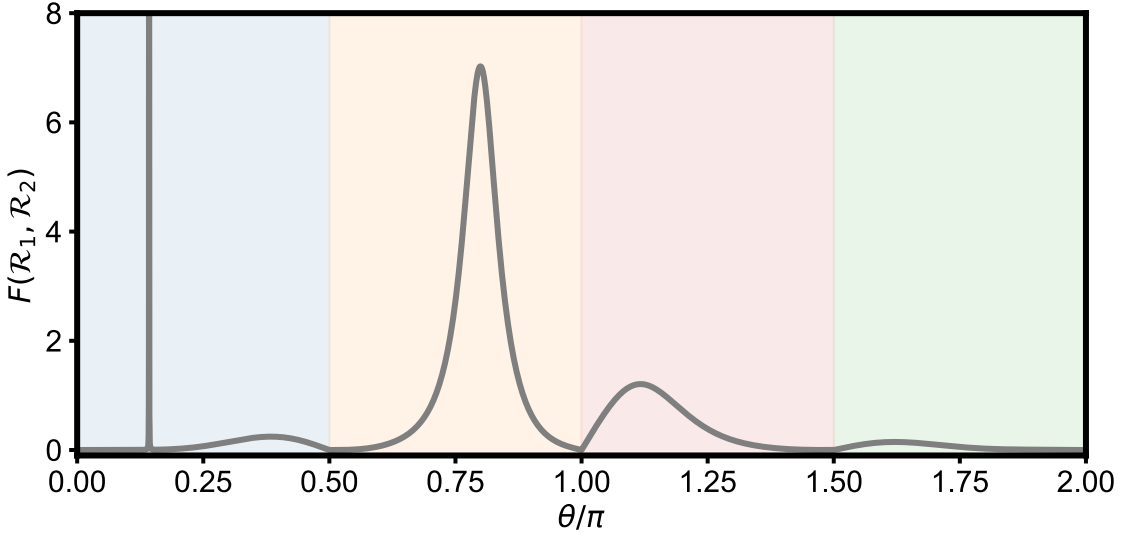


FIG. S10: $F(\mathcal{R}_1, \mathcal{R}_2)$ along the four edges. Areas with different background colors correspond to the four edges.

S8 . NON-RECIPROCITY OF THE PHOTON TRANSMISION

In the regime $\lambda_2 \ll \lambda_1, \kappa$, the strong Q - R_r coupling produces two dressed eigenstates, $|\Psi'_{\pm}\rangle = |0_b\rangle|\Phi'_{\pm}\rangle$, where $|\Phi'_{\pm}\rangle$ are given by Eq. (S23). In terms of these dressed states, the three-partite NH Hamiltonian can be rewritten as

$$H = E'_+ |\Psi'_+\rangle \langle \Psi'_+| + E'_- |\Psi'_-\rangle \langle \Psi'_-| + (\varepsilon_+ |\Psi'_+\rangle - \varepsilon_- |\Psi'_-\rangle) \langle 1_b 0_q 0_r|, \quad (\text{S46})$$

where

$$\begin{aligned} \varepsilon_+ &= \frac{\lambda_1}{\lambda_2/E'_+ - \lambda_2/E'_-} \frac{\lambda_2}{\mathcal{N}_+ E'_+}, \\ \varepsilon_- &= \frac{\lambda_1}{\lambda_2/E'_+ - \lambda_2/E'_-} \frac{\lambda_2}{\mathcal{N}_- E'_-}. \end{aligned} \quad (\text{S47})$$

When the Q - R_b coupling strength λ_2 is sufficiently weak, the magnitudes of the energy gaps between $|1_b 0_q 0_r\rangle$ and the two dressed states $|E'_{\pm}\rangle$ are much larger than the corresponding couplings ε_{\pm} .

If the photon is initially stored in R_b , the large energy gaps $|E'_{\pm}|$ suppresses the populations of $|\Psi'_{\pm}\rangle$, freezing the system evolution. In other words, the photon only has a slight probability of being transferred to Q due to the large detunings. Once this occurs, the strong Q - R_r coupling, together with the strong dissipation, makes the photon quickly leak to the environment. This is confirmed by the result presented in Fig. 4a of the main text, which is in good agreement with the numerical simulation of the population evolutions for the states $|1_b 0_q 0_r\rangle$, $|0_b 1_q 0_r\rangle$, and $|0_b 0_q 1_r\rangle$. When the photon is initially stored in R_r , it leaks through two channels: escape to the environment and be transmitted to R_b through Q . Once the photon has been transferred to R_b , it stays there and cannot return to the Q - R_r subsystem due to the large detunings. The population accumulation in R_b , together with the irreversible photon loss in R_r , makes the ratio between the populations of $|1_b 0_q 0_r\rangle$ and $|0_b 0_q 1_r\rangle$ monotonously increase, as evidenced by the result displayed in Fig. 4b of the main text, which agrees well with the numerical result.